Stable three-axis nuclear-spin gyroscope in diamond

Ashok Ajoy and Paola Cappellaro
Department of Nuclear Science and Engineering and Research Laboratory of Electronics, Massachusetts Institute of Technology, Cambridge, Massachusetts 02139, USA
(Received 29 May 2012; published 11 December 2012)

Gyroscopes find wide applications in everyday life from navigation and inertial sensing to rotation sensors in hand-held devices and automobiles. Current devices, based on either atomic or solid-state systems, impose a choice between long-time stability and high sensitivity in a miniaturized system. Here, we introduce a quantum sensor that overcomes these limitations by providing a sensitive and stable three-axis gyroscope in the solid state. We achieve high sensitivity by exploiting the long coherence time of the ^{14}N nuclear spin associated with the nitrogen-vacancy center in diamond, combined with the efficient polarization and measurement of its electronic spin. Although the gyroscope is based on a simple Ramsey interferometry scheme, we use coherent control of the quantum sensor to improve its coherence time and robustness against long-time drifts. Such a sensor can achieve a sensitivity of $\eta \sim 0.5\ (\text{mdeg s}^{-1})/\sqrt{\text{Hz mm}^3}$ while offering enhanced stability in a small footprint. In addition, we exploit the four axes of delocalization of the nitrogen-vacancy center to measure not only the rate of rotation, but also its direction, thus obtaining a compact three-axis gyroscope.

DOI: 10.1103/PhysRevA.86.062104 PACS number(s): 03.65.Vf, 06.30.Gv, 61.72.jn

I. INTRODUCTION

Conventional commercial gyroscopes are built using microelectromechanical systems (MEMS) technology that allows for sensitivities exceeding $3\ (\text{mdeg s}^{-1})/\sqrt{\text{Hz}}$ in a hundreds of micron-sized footprint [1,2]. Despite several advantages—including low current drives ($\sim 100\ \mu$A) and large bandwidths ($\gtrsim 200$ deg/s)—that have allowed MEMS gyroscopes to gain ubiquitous usage, they suffer from one critical drawback: The sensitivity drifts after a few minutes of operation, making them unattractive for geodetic applications [3]. The intrinsic reason for these drifts—formation of charged asperities at the surface of the capacitive transduction mechanism—is endemic to MEMS but does not occur in other systems used as gyroscopes, such as atom interferometers [4–6] or nuclear spins [7–9]. However, to achieve sensitivities comparable to MEMS, these systems require large volumes ($\sim$cm^3), long startup times, and large power and space overheads for excitation and detection.

Here, we propose to overcome the drawbacks of these two classes of gyroscopes by using a *solid-state* spin gyroscope (that we call an *nNV gyro*) associated with the nuclear spin of nitrogen-vacancy (NV) [10] centers in diamond (Fig. 1). The *nNV gyro* combines the efficient optical initialization and measurement offered by the NV-electronic spin with the stability and long coherence time of the nuclear spin, which is preserved even at high densities.

The operating principles are based on the detection of the phase[1] that the nitrogen-14 nuclear spin 1 acquires when it rotates around its symmetry axis. Consider an isolated spin 1 with Hamiltonian $\mathcal{H}_0 = QI_z^2 + \gamma_N b I_z$, where Q is the intrinsic quadrupolar interaction ($Q = -4.95$ MHz for the NV center's ^{14}N), b is a small magnetic field, $\gamma_N b \ll Q$, and $\gamma_N = 2\pi \times 3.1$ MHz/T is the ^{14}N gyromagnetic ratio. The spin is subject to rf fields in the transverse plane at frequency Q and with a (gated) amplitude $2\omega_{\text{rf}}(t)$. The diamond rotates around the spin-symmetry axis (z axis) at a rate Ω with respect to the frame in which the rf field is applied. Thus, the driving field is described by the Hamiltonian $\mathcal{H}_{\text{rf}} = 2\omega_{\text{rf}}(t)\cos(Qt)[I_x\cos(\Omega t) - I_y\sin(\Omega t)]$. We can describe the spin evolution in the interaction frame set by $(QI_z^2 - \Omega I_z)$. The second term $(e^{-i\Omega I_z})$ transforms $\mathcal{H}_{\text{rf}}$ to

$$2\omega_{\text{rf}}\cos(Qt)I_x = \omega_{\text{rf}}\left[e^{-iQI_z^2 t}I_x e^{iQI_z^2 t} + e^{iQI_z^2 t}I_x e^{-iQI_z^2 t}\right],$$

thus, in the rotating-wave approximation, the dynamics is governed by the Hamiltonian,

$$\mathcal{H}_I = (\gamma_N b + \Omega)I_z + \omega_{\text{rf}}(t)I_x. \tag{1}$$

In a Ramsey sequence (Fig. 2), the spin acquires a phase $\varphi = (\gamma_N b + \Omega)t$ from which one can extract the rotation rate.

Although the nNV-gyro operating principles are somewhat similar to NV-based magnetometers [12] and NMR gyroscopes [9], some critical differences lead to its outstanding performance. In contrast to magnetometry, the sensitivity to rotation rates is independent of the spin's gyromagnetic ratio. Thus, we can exploit the ^{14}N nuclear spin as a sensor, leading to a much improved performance because of the isolation of nuclear spins from noise sources. However, this also requires new strategies for the polarization and readout of the nuclear spin, which we illustrate below. There are two critical advantages of the nNV gyro with respect to NMR gyros. Although certain NMR-gyroscope designs use optical pumping for spin polarization [13,14], the nNV gyro exploits the unique properties of the NV electron spin for optical polarization and readout of the nuclear spins, achieving far better efficiencies, close to 100%. Furthermore, using a solid-state system allows the application of control fields in the *same* reference frame of the sensor spins, which, as we show below, decouple the spins from low-frequency noise sources, such as temperature fluctuations, stray magnetic fields, and strains. Stated equivalently, whereas NMR gyros are limited by the *dephasing* time T_2^* of the spins, the nNV gyro is limited by the much longer *coherence* time T_2. In the following, we

[1]While this paper was in preparation, a proposal to utilize the *geometric* phase acquired by the electronic NV spin as a rotation sensor appeared in Refs. [56,57].

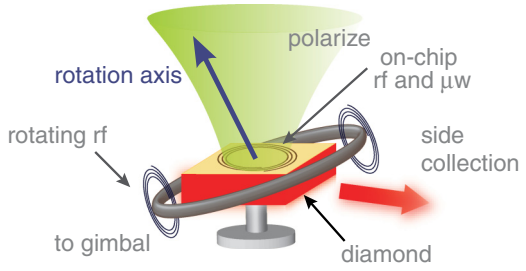

FIG. 1. (Color online) *Conceptual design of the nNV gyro.* A slab of diamond of dimensions (2.5×2.5) mm^2 $\times$ 150 μm is anchored to the device body. Radio-frequency (rf) coils and microwave (μw) co-planar waveguides are fabricated on the diamond for fast control. NV centers are polarized by a green laser (532 nm), and state-dependent fluorescence intensity (637 nm) is collected employing a side-collection technique [11]. A second set of rf coils rotate with respect to the diamond-chip frame, for example, by being attached to one or more rings in a mechanical gimbal gyroscope (not shown). The ^{14}N nuclear spins are used as probes of the *relative* rotation between the diamond frame and the external rf-coil frame. See Fig. 5 for a possible actual implementation.

present details of the nNV-gyro operation and analyze its expected performance.

II. GYROSCOPE OPERATION

Consider first the operation of a one-axis nNV gyro. The nuclear spin is first initialized by polarization transfer from the electronic NV spin. Under optical excitation, the electronic $m_s = \pm 1$ levels follow a non-spin-preserving transition through metastable levels down to the $m_s = 0$ ground state, yielding high polarization of the electronic spin [15,16]. The polarization can be transferred to the nuclear spin exploiting the hyperfine coupling $A = 2.2$ MHz in the electron-nuclear-spin Hamiltonian,

$$\mathcal{H}_{en} = \Delta S_z^2 + \gamma_e b S_z + Q I_z^2 + (\Omega + \gamma_N b) I_z + A \vec{S} \cdot \vec{I}, \quad (2)$$

where $\gamma_e = 2.8$ MHz/G is the electronic gyromagnetic ratio and $\Delta = 2.87$ GHz is the zero-field splitting. Several methods

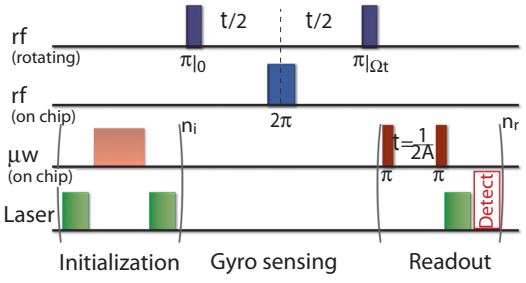

FIG. 2. (Color online) *nNV-gyro control sequence.* rf pulses, resonant with the quadrupolar transition of the ^{14}N nuclear spin, are applied in a frame rotating at a rate Ω with respect to the diamond, thus, inducing a phase Ωt. The nuclear spin is first initialized by polarization transfer from the NV-electronic spin. An echo pulse is applied in the diamond frame to refocus static frequency shifts. Finally, Ω is extracted by mapping the nuclear-spin phase shift onto a population difference of the electronic spin and measuring the corresponding fluorescence intensity.

for polarization transfer have been implemented experimentally, including measurement postselection [17] and exploiting a level anticrossing in the orbital excited state at $b \sim 500$ G (using an adiabatic passage [18] or the resonance between the nuclear and the electronic spins [19–21]). Unfortunately, all these methods have drawbacks that make them unsuitable for our purpose. The first method is too lengthy, whereas the second prevents the use of repeated readouts and requires precise alignment of a large static magnetic field. At low field, polarization transfer between the electronic and the nuclear spins is complicated by the fact that both are spin 1. Unlike for spin 1/2, polarization transfer in the rotating frame (under the Hartmann-Hahn-matching condition [22]) does not lead to perfect polarization, unless the electronic spin is reduced to an effective spin 1/2 [23]. Instead, here, we propose using forbidden two-photon transitions to achieve population transfer. Driving the NV-electronic spin at the $\Delta \pm \gamma_e b + Q$ transitions with a field along its *longitudinal* (z) axis [24] modulates its resonance frequency, thus, making energy exchange with the nuclear spin possible. This is similar to two-photon transitions described by Floquet theory [25]: Although the transition rates are usually small, the ability to drive the NV-electronic spin with very high fields [26] makes the polarization time $t = \pi \frac{\Delta + \gamma_e b + Q}{A \Omega_R}$ short: For a Rabi frequency $\Omega_R = 500$ MHz and a field $b = 20$ G, the time required is only 1.3 μs (see Appendix A). We note that this initialization time is far shorter than for other gyroscope types, including the few tens of milliseconds of startup time required for MEMS gyroscopes [1].

For ease of operation, we assume that the rf and μw pulses used for initialization and readout can be delivered by an on-chip circuit, integrated with the diamond. After preparation, the NV-electronic spin is left in the $|0\rangle$ state, which does not couple to the ^{14}N nuclear spin nor to the spin bath. A Ramsey sequence is applied using the off-chip rf driving, thus, inducing accumulation of a rotation-dependent phase [Eq. (1)]. A 2π pulse at the center of the sequence, applied with the on-chip rf field, refocuses the effects of stray magnetic fields and provides decoupling from the spin bath.[2] The sensor spin coherence time is limited by T_2 (and not by the shorter dephasing time T_2^*), which can be exceptionally long for nuclear spins. Thus, the additional pulse, made possible by working with a solid-state device, is critical in making the nNV gyro immune to a host of low-frequency drifts that limit the operational time of other gyroscope types.

Moreover, since the echo refocuses the coupling to other electronic spins, the nNV gyro can operate at very high densities of the sensor spins. Ion implantation can reach an NV density of $n_{\rm NV} \sim 10^{18}$ cm^{-3}. Even assuming a density of residual single-nitrogen defects (P1 centers [27,28]) $n_{\rm P1} \approx 10 n_{\rm NV} \sim 10^{19}$ cm^{-3}, the ^{14}N T_2 time is not appreciably affected by the P1 bath. Indeed, while at these densities, the dipole-dipole interaction $d_{ab} = \frac{\mu_0}{4\pi} \frac{\hbar}{2\pi} \frac{\gamma_a \gamma_b}{r_{ab}^3}$ among P1 centers is large ($d_{\rm P1,P1} \sim 3$ MHz with $\gamma_{\rm P1} = \gamma_e$), and the coupling to the nuclear spin is still small, $d_{P1,N} \sim 345$ Hz (where we

[2]The echo is effective, even if the on- and off-chip fields cannot be made phase coherent.

estimated the mean-spin-spin distance as $r = \sqrt[3]{\ln(8)/(4\pi n_{\mathrm{P1}})}$ [29]). This leads to motional narrowing and a very slow exponential decay as confirmed by simulations (Appendix B). The ^{14}N coherence time is also affected by the interaction with the close-by NV center [17,18], which induces dephasing when undergoing relaxation with $T_1 \sim 2$–6 ms at room temperature and low field [30]. Whereas, in high-purity diamonds, the dephasing time T_2^* can be as long as 7 ms [17], in the proposed conditions of operation, we can conservatively estimate the coherence time of the nuclear spin to be $T_2 = 1$ ms. We note that the echo sequence has the added benefit to make the measurement insensitive to many other imperfections, such as temperature variation, strain, background stray fields, variation in the quadrupolar interaction, and instability in the applied bias magnetic field. Thus, this scheme yields a solid-state gyroscope with stability comparable to that achieved in atomic systems.

After the sensing sequence, the ^{14}N spin is left in the state,

$$|\psi_n\rangle = \frac{\sin(\Omega t)}{\sqrt{2}}(e^{+i\Omega t}|-1\rangle - e^{-i\Omega t}|+1\rangle) - \cos(\Omega t)|0\rangle, \tag{3}$$

which can be mapped into a population difference between the NV levels thanks to the hyperfine coupling (here, we only consider the longitudinal component of the isotropic hyperfine interaction AI_zS_z because of the large zero-field splitting Δ).

The readout sequence (Fig. 2), with pulses on resonance to both $0 \leftrightarrow \pm 1$ transitions,[3] generates the state,

$$|\psi_{en}\rangle = \frac{1}{2}\sin(\Omega t)[e^{i\Omega t}(|-1,-1\rangle + |+1,-1\rangle) + e^{-i\Omega t}(|+1,+1\rangle + |-1,+1\rangle)] - \cos(\Omega t)|0,0\rangle, \tag{4}$$

where $|m_z^S, m_z^I\rangle$ indicates an eigenstate of S_z and I_z for the electronic and nuclear spins, respectively. The time required to map the state onto the NV center is $t_{\mathrm{map}} = 230$ ns, which is close to the T_2^* time for the NV at high densities, thus, we expect a reduction in contrast. Indeed, it is the NV dephasing time that ultimately limits the allowed spin densities. A possible solution would be to perform a spin echo on both nuclear and electronic spins to extend the coherence time.

Optical readout extracts the information about the rotation Ω. The measurement step can be repeated to improve the contrast [31,32]: Although, at low field, the nuclear-spin relaxation time under optical illumination is relatively short, thus, limiting the number of repeated readouts [31] when combined with a side-collection scheme [11] giving high collection efficiency $\eta_m \approx 1$, we can still achieve a detection efficiency of $C \sim 0.25$ for $n_r = 100$ repetitions and a total readout time of $t_{\mathrm{ro}} \approx 150\ \mu$s (see Appendix C). The higher detection efficiency will also allow a large dynamic range by exploiting adaptive phase-estimation schemes [17,33,34].

[3]The mapping is also possible if only one NV transition is driven, although it requires a longer time.

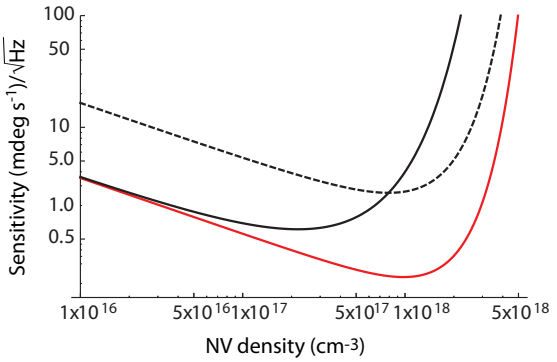

FIG. 3. (Color online) *nNV-gyro sensitivity* in (mdeg s^{-1})/$\sqrt{\mathrm{Hz}}$ as a function of density $\eta(n) = \frac{e^{t_{\mathrm{map}}/T_{2,\mathrm{NV}}^*} e^{t/T_{2,n}}}{C\sqrt{nV/4}} \frac{\sqrt{t+t_d}}{t}$. Here, the exponential factors take into account the sensitivity degradation due to spin decoherence [12] with decay constants that depend on density, $T_{2,n}, T_{2,\mathrm{NV}}^* \propto 1/n$ (Appendix B). We considered a diamond chip of dimensions $V = (2.5 \times 2.5)$ mm$^2 \times 150\ \mu$m and assumed that only 1/4 of the NV spins were along the desired direction. The interrogation times were $t = 1$ ms (solid lines) and $t = 0.1$ ms (dashed line). The sensitivity for a simple Ramsey scheme (black lines) is limited by the nuclear spin $T_{2,n} = T_2^*$. Using an echo scheme (red thick line) improves the sensitivity, which is now limited by the coherence time $T_{2,\mathrm{NV}}^*$ of the NV-electronic spin used to read out the sensor spin state since the nuclear coherence time $T_{2,n} = T_2$ is much longer.

III. PERFORMANCE OF nNV GYROSCOPES

We now consider the performance of the nNV-gyroscope design with respect to sensitivity and stability and its potential advantages over competing technologies.

The sensitivity per unit time η is ideally shot-noise limited [12,35]: $\eta \propto 1/\sqrt{tN}$, where N is the number of nitrogen nuclear spins associated with NV centers in the diamond chip. We estimate the expected sensitivity by limiting the interrogation time t to T_2 and taking into consideration the preparation and readout dead times $t_d = t_{\mathrm{pol}} + t_{\mathrm{ro}}$ and the detection efficiency C,

$$\eta = \frac{\sqrt{T_2 + t_d}}{CT_2\sqrt{N}}. \tag{5}$$

For a volume $V = 1$ mm^3, containing $N = n_{\mathrm{NV}}V/4 \approx 2.5 \times 10^{14}$ sensor spins along the rotation axis, the estimated sensitivity for the nNV gyro is then $\eta \approx 0.5$ (mdeg s^{-1})/$\sqrt{\mathrm{Hz}}$, better than the current MEMS gyroscopes, although in a slightly larger volume (see Fig. 3).

More importantly, the *stability* of the nNV gyro can be much higher than for MEMS and can be comparable to atomic gyroscopes (see Table I). Indeed, the echo-based scheme makes the nNV gyro insensitive to drifts due to strain, temperature, and stray fields. In addition, the NV spin is a sensitive probe of these effects, capable of measuring magnetic [12] and electric [36] fields as well as frequency [37] and temperature shifts [38]. Because of almost 4 orders of magnitude larger sensitivity of the NV spin than the ^{14}N spin (given by the ratio γ_e/γ_N), the NV can be used to monitor such drifts and to correct them via a feedback mechanism.

TABLE I. Representative examples from different gyroscope families showing their typical performance parameters. S/G in the first column indicates whether the gyroscope is solid state (S) or gas based (G). Note that there is, in general, a wide variance in parameters in each gyroscope family; here, we just show typical examples. Moreover, laboratory-based gyroscope setups may not be optimized for compact sizes.

Gyroscope type	Size (mm^3)	Sensitivity ($deg/\sqrt{h}$)	Startup time
Fiber optic (S) [39]	3.6×10^4	0.5	250 ms
Ring laser (G) [40]	1×10^6	3.5×10^{-3}	1 s
Cold atoms (G) [41]	$\sim 10^9$	2.95×10^{-4}	51 ms
Atom beam (G) [7]	1.56×10^4	2×10^{-3}	
MEMS (S) [1]	147	1.6	50 ms
NMR (G) [9,42]	$>10^3$	10^{-3}	100 s
nNV gyro (S)	1[a]	3×10^{-2}	1.3 μs

[a]This is the active sensing volume.

IV. OPERATION OF THE nNV GYRO AS A THREE-AXIS GYROSCOPE

The NV center in diamond consists of a substitutional nitrogen adjacent to a vacancy in the lattice. The nitrogen-to-vacancy axis sets the direction of the electronic zero-field splitting and nuclear quadrupolar interaction. The axis can be along any of the four tetrahedral $\langle 111 \rangle$ crystallographic directions of the diamond lattice. This intrinsic symmetry can be exploited to operate the nNV gyro as a three-axis gyroscope, extracting information about the rotation rate as well as its direction.

Although the maximum sensitivity is achieved for rotations aligned with the symmetry axis, if the rotation $\vec{\Omega}$ is about an axis forming an angle $\{\theta,\phi\}$ with respect to the NV axis, the ^{14}N still undergoes a complex evolution that depends on $\vec{\Omega}$. The two rf pulses in the Ramsey interferometry scheme differ not only by their phase $\psi_{1,2}$ in the NV x-y plane, but also by their flip angle $\alpha_{1,2}$. If we assume the first pulse to be along the x axis for the first NV class, the second rf pulse is rotated by an angle $\psi_2^1 = \psi(\theta,\phi,\Omega t)$ in the NV x-y plane with

$$\tan\left(\psi_2^1\right) = \frac{\sin^2\theta\ \sin(2\phi)\sin^2(\Omega t/2) + \cos\ \theta\ \sin(\Omega t)}{\cos(\Omega t) - \sin^2\theta\ \cos^2\phi\ \cos(\Omega t) + \sin^2\theta\ \cos^2\phi}.$$

The flip angle $\alpha_2^1 = \alpha(\theta,\phi,\Omega t)$ is also reduced with respect to the nominal angle π,

$$\alpha_2^1 = \pi[\{\cos(\Omega t) - \sin^2\theta\ \cos^2\phi\ \cos(\Omega t) + \sin^2\theta\ \cos^2\phi\}^2 + \{\sin^2\theta\ \sin(2\phi)\sin^2(\Omega t/2) + \cos\ \theta\ \sin(\Omega t)\}^2]^{1/2}.$$

The state at the end of the Ramsey sequence is then given by

$$|\psi_n\rangle = \frac{e^{-i\psi_2}\left[\sin(\psi_2) - i\ \cos\left(\frac{\alpha_2}{2}\right)\cos(\psi_2)\right]}{\sqrt{2}}|+1\rangle - \sin\left(\frac{\alpha_2}{2}\right)\cos(\psi_2)|0\rangle - \frac{e^{i\psi_2}\left[\sin(\psi_2) + i\ \cos\left(\frac{\alpha_2}{2}\right)\cos(\psi_2)\right]}{\sqrt{2}}|-1\rangle,$$

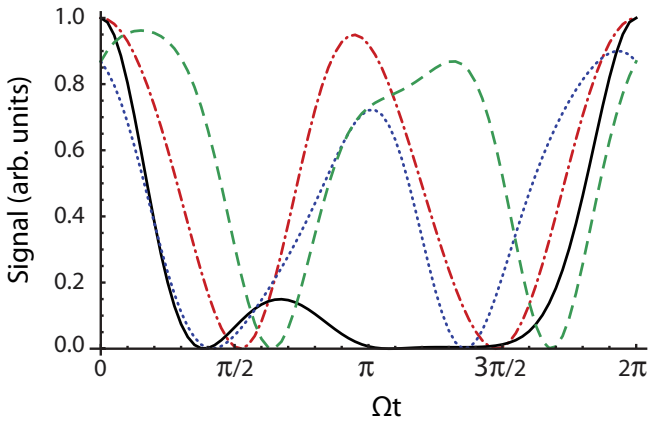

FIG. 4. (Color online) Signal S_c from the four classes of NV centers for a rotation Ω along an axis with angles $\theta = \pi/6$ and $\phi = 2\pi/3$ from the [111] direction (which coincides with the first class of NVs, dashed-dotted line).

from which one can extract information about the rotation rate Ω. Similar expressions hold for the other NV classes if it is possible to drive excitation fields in the transverse plane of each family. Then, the angles α_2^c, ψ_2^c are different for each family of NVs, and measuring the signal from three families allows extracting information about $\vec{\Omega}$.

Assuming that the driving field is applied only along one direction for all the four NV classes, even the first excitation pulse angles $\{\psi_1^c,\alpha_1^c\}$ differ for each class, whereas, for the second pulse, $\{\psi_2^c,\alpha_2^c\}$ depend not only on the class, but also on the rotation vector $\vec{\Omega}$ via simple trigonometric relationships. We, thus, obtain the signal for each class,

$$S^c = \left[\cos\left(\alpha_1^c/2\right)\cos\left(\alpha_2^c/2\right) - \sin\left(\alpha_1^c/2\right)\sin\left(\alpha_2^c/2\right)\cos\left(\psi_1^c - \psi_2^c\right)\right]^2, \quad (6)$$

which is shown in Fig. 4. The signal can be measured by sequentially mapping the nuclear-spin state onto the corresponding electronic spin via on resonance microwave pulses (a bias field of 10–20 G is sufficient to lift the frequency degeneracy among the four classes [43,44]). A more efficient scheme would take advantage of repeated readouts and long relaxation times of the nuclear spins to measure the signal from three NV classes without the need to repeat the preparation and echo sequences. Although a driving field along a single direction makes the deconvolution algorithm more complex, the signal arising from three classes of NV centers is still enough to reconstruct the rotation rate and its direction.

V. CONCLUSION

We proposed a solid-state device able to measure rotation rates with a resolution of $\eta \approx 0.5\ (\text{mdeg}\,\text{s}^{-1})/\sqrt{\text{Hz}}$ in a 1-mm^3 package while providing great stability. The device performance compares favorably with respect to other current technologies (see Table I). Even smaller devices—on the micron scale—could be useful by exploiting this long-time stability to improve the performance of the MEMS gyroscope in a combinatoric device (see Fig. 5). High-performance MEMS gyroscopes can be fabricated in diamond using reactive-ion-etching tools [45]. While the substrate itself acts as a

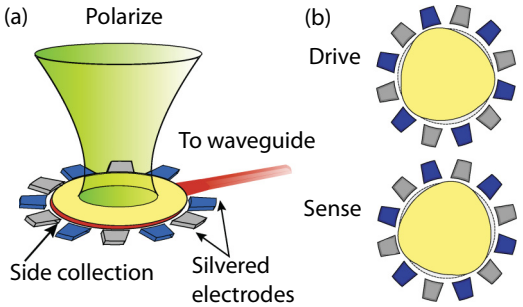

FIG. 5. (Color online) *Conceptual design of an integrated nNV-MEMS gyroscope*, comprising a bulk acoustic wave (BAW) single-axis MEMS gyroscope [2] in an ∼800-μm diamond disk implanted with NV centers, whose nuclear spins form a spin gyroscope. (a) Schematic of the nNV-gyro operation. The spins implanted in the disk are polarized by an on-chip green laser. The electrodes surrounding the disk are silvered to allow for total internal reflection, and fluorescence is side collected [11] by replacing one of them by an on-chip optical waveguide at 638 nm. Strip lines for rf or μw control are fabricated on the disk. (b) Operation of the BAW mechanical gyroscope. The BAW is *electrostatically* driven in the second elliptic mode by an ∼10-kHz sinusoidal signal from the *drive* (blue) electrodes. A rotation out of the plane causes a decrease in the gap near the *sense* (grey) electrodes, leading to a capacitive measurement of the rotation [2]. Combinatoric filtering with the nNV measurement leads to noise rejection and improved stability.

mechanical gyroscope, the nuclear spins inside it act as a *spin* gyroscope. These two gyroscopes, employing complementary physical effects, are sensitive to different sources of noise, which can be corrected by Kalman-filter techniques [46]. The integrated device would offer both stability and sensitivity in a small package.

The nNV gyro takes full advantage of the long coherence time of *nuclear* spins, which is preserved even at very high densities while exploiting its interaction with the electronic spin of the NV center for efficient initialization and readout. Going beyond our conservative estimates, the nNV gyro could achieve the performance of inertial-grade gyroscopes with improvements in the coherence time of the nuclear- and electronic-NV spins as could be obtained with $\gtrsim$50% N-to-NV conversion efficiency [47] with a preferential alignment of the NV-symmetry axis along two directions [48] and with improved collection efficiency, exploiting the single-shot measurement of the NV center at low temperatures [49,50].

ACKNOWLEDGMENTS

It is a pleasure to thank S. Bhave for stimulating discussions and encouragement. We thank J. Hodges for discussions. This work was supported, in part, by the US Army Research Office through a MURI Grant No. W911NF-11-1-0400.

APPENDIX A: POLARIZATION SCHEME FOR THE ^{14}N NUCLEAR SPIN

In the main text, we proposed using two-photon transitions to drive polarization transfer between the electronic and the nuclear spins associated with the NV center. These transitions can be accessed by driving the NV-electronic spin at the $\omega_\pm = \Delta \pm \gamma b + Q$ frequencies with a field *along* its longitudinal (z) axis [24,51]. The longitudinal field effectively modulates the electronic spin-resonance frequency, thus, making energy exchange with the nuclear spin possible. Consider the Hamiltonian in Eq. (2). In the interaction frame given by $\mathcal{H}_I = \mathcal{H}_{en} - A\vec{S}\cdot\vec{I}$, the coupling term acquires a time dependence. For example, the term $\mathcal{H}_p = A(|0\rangle\langle+1|_e|0\rangle\langle-1|_n + \text{H.c.})$, which drives the polarization exchange, acquires a phase oscillating at the frequency $\pm(\Delta + \gamma b + Q)$. Adding a longitudinal field $\mathcal{H}_z = \Omega\cos(\omega_+ t)S_z$ further modulates the time dependence when evaluating the Hamiltonian in the corresponding interaction picture given by $U_z = e^{i\Omega\sin(\omega_+ t)/\omega_+ S_z}$. For the terms considered above, we have, for example,

$$\begin{aligned}\widetilde{\mathcal{H}}_p &= A(e^{-i[\omega_+ t - \Omega\sin(\omega_+ t)/\omega_+]}|0\rangle\langle1|_e|0\rangle\langle-1|_n + \text{H.c.})\\ &= A\left(\sum_n J_n\left(\frac{\Omega}{\omega_+}\right)e^{-i\omega_+(1-n)t}|0\rangle\langle1|_e|0\rangle\langle-1|_n + \text{H.c.}\right),\end{aligned}$$

where we used the properties of the Bessel function $J_n(\cdot)$. In the rotating-wave approximation, only the term $n = 1$ is retained, while all the other terms in the Hamiltonian $\widetilde{\mathcal{H}}_I$ that oscillate at a frequency $\neq\omega_+$ are also canceled. In the limit $\Omega \ll \omega_+$, we have $J_n(\Omega/\omega_+) \approx \Omega/(2\omega_+)$, thus, the Hamiltonian-inducing polarization exchange is $\mathcal{H}_p \approx \frac{A\Omega}{2\omega}(|0\rangle\langle1|_e|0\rangle\langle-1|_n + \text{H.c.})$.

The ability to drive the NV-electronic spin with very high fields [26] makes the polarization time $t = \pi\frac{\Delta+\gamma b+Q}{A\Omega_R}$ short: For a Rabi frequency $\Omega_R = 500$ MHz, hyperfine $A \approx 2.2$ MHz, and a field of 20 G, the time required is only 1.3 μs; thus, the forbidden transition is a competitive way of driving nuclear-spin transitions. Given the short dephasing time of the NV spin, a two-step process might be required in which the NV is optically repolarized before driving the polarization exchange a second time. To estimate the effects of a spin bath during the longitudinal driving, we simulated the polarization transfer in the presence of dephasing noise (see Fig. 6).

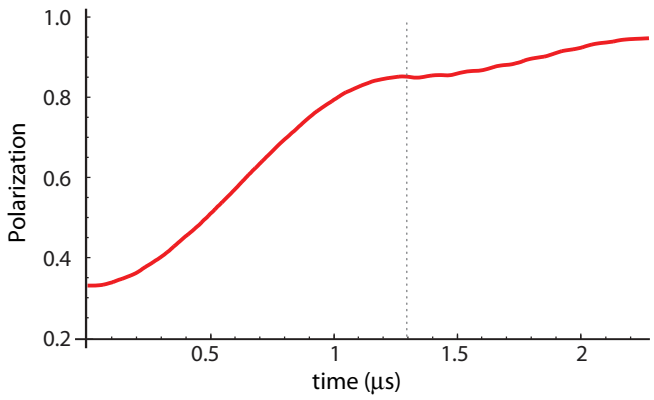

FIG. 6. (Color online) Polarization of the ^{14}N nuclear spin under longitudinal driving of the NV-electronic transitions with a Rabi frequency of $\Omega_R = 500$ MHz, hyperfine $A \approx 2.2$ MHz, and a static magnetic field of 20 G. The simulation includes dephasing of the electronic spin modeled by an Ornstein-Uhlenbeck process, yielding a T_2^* time of about 200 ns. To achieve high polarization, the process is repeated twice by repolarizing the NV-electronic spin (dashed line) via optical illumination.

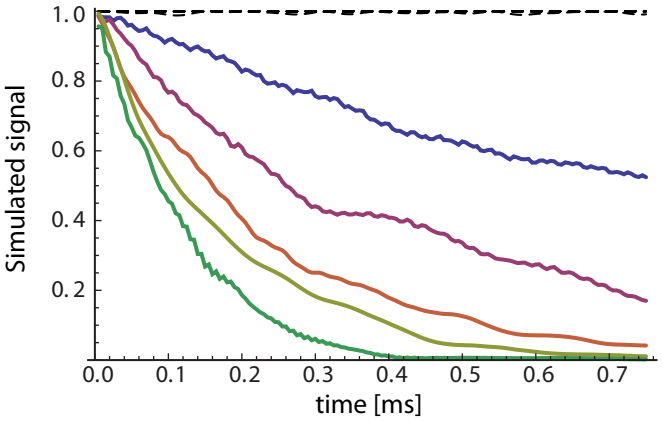

FIG. 7. (Color online) ^{14}N coherence decay under a spin-echo sequence (black, dashed lines) and a Ramsey sequence (solid lines). We simulated an ensemble of 100 noninteracting nuclear spins, each subjected to a bath of $\sim$500 electronic spins with a density (from bottom to top lines) of $n = (0.35, 1.06, 1.76, 2.47, 3.17) \times 10^{19}$ cm^{-3}. (The lines for the echo are indistinguishable.)

APPENDIX B: COHERENCE TIME OF THE ^{14}N NUCLEAR SPINS

The ^{14}N nuclear-spin dephasing and coherence time are usually limited by the T_1 relaxation time of the electronic NV spin. At a high density of paramagnetic impurities, the interaction with other electronic spins could accelerate the decay. To estimate this contribution, we simulated the ^{14}N nuclear-spin evolution under a Ramsey and echo sequence in the presence of an electronic-spin bath. The simulation was performed using a cluster expansion [52,53] to model the effects of a P1 electronic-spin bath. The spin bath was modeled as an ensemble of electronic-spin $1/2$, thus, omitting the details of the actual bath (such as the strong hyperfine coupling of the P1 to its nuclear spins as well as shielding effects due to nearby carbon-13 nuclear spins [54] and localization effects due to disorder [55]). Still, the simulations can give rough estimates of the expected T_2 times and are consistent with the results of a simple model based on describing the spin bath as a classically fluctuating bath described by an Ornstein-Uhlenbeck process. In particular, we expect that, due to motional narrowing, the coherence times are long even at high densities as shown in Fig. 7.

APPENDIX C: IMPROVED MEASUREMENT EFFICIENCY BY REPEATED READOUTS

The NV-spin state can be read under nonresonant illumination at room temperature using the fact that the $m_s = \pm 1$ excited states can decay into metastable states, which live for $\sim$300 ns. The optical excitation conserves spin as does the direct optical decay, which happens in about 12 ns. Thus, an NV in the $m_s = 0$ state will emit and will absorb approximately 15 photons, compared to only a few for an NV in the $m_s = \pm 1$ states, yielding state discrimination by fluorescence intensity. The complication is that the metastable state decays primarily via spin-non-conserving processes into the $m_s = 0$ state, thereby reorienting the spin. This is good for spin polarization but erases the spin memory and reduces measurement contrast. The detection efficiency of the NV-center spin state is, thus, given by $C = (1 + \frac{2(n_0+n_1)}{(n_0-n_1)^2})^{-1/2}$ [12], where $n_{1,0}$ is the number of photons collected if the NV spin is in the $m_s = \{0,1\}$ state, respectively.

In the repeated readout scheme [31,32], the state of the nuclear spin is repetitively mapped onto the electronic spin, which is then read out under laser illumination. The measurement projects the nuclear-spin state into a mixed state, but the information about its population difference is preserved under the assumption that the measurement is a good quantum nondemolition measurement. We can include the effect of these repeated readouts by defining a new detection efficiency $C_{n_r} = (1 + \frac{2(n_0+n_1)}{n_r(n_0-n_1)^2})^{-1/2}$, which shows an improvement $\propto \sqrt{n_r}$, where n_r is the number of measurements. The sensitivity needs, of course, to be further modified to take into account the increased measurement time. Provided the time needed for one measurement step is smaller than the interrogation time (including the initialization time), it becomes advantageous to use repeated readouts. The maximum number of readouts is set by the nuclear-spin relaxation under optical illumination, driven by non-energy-conserving flip-flops in the excited states. While at high fields, this time is very long, allowing 2000 measurements in 5 ms, in the present conditions, we find that $\sim$100 measurements would provide a good balance between the improvement in C and the reduction due to longer measurement times.

[1] *ADXRS624 Data Sheet Rev A* (Analog Devices, Norwood, MA), http://www.analog.com/static/imported-files/data_sheets/ADXRS624.pdf.

[2] H. Johari, J. Shah, and F. Ayazi, in *IEEE 21st International Conference on Micro Electro Mechanical Systems, 2008. MEMS 2008* (IEEE, Piscataway, NJ, 2008), pp. 856–859.

[3] C. Jekeli, *Inertial Navigation Systems with Geodetic Applications* (de Gruyter, New York, 2000).

[4] A. Lenef, T. D. Hammond, E. T. Smith, M. S. Chapman, R. A. Rubenstein, and D. E. Pritchard, Phys. Rev. Lett. **78**, 760 (1997).

[5] T. L. Gustavson, P. Bouyer, and M. A. Kasevich, Phys. Rev. Lett. **78**, 2046 (1997).

[6] D. S. Durfee, Y. K. Shaham, and M. A. Kasevich, Phys. Rev. Lett. **97**, 240801 (2006).

[7] T. W. Kornack, R. K. Ghosh, and M. V. Romalis, Phys. Rev. Lett. **95**, 230801 (2005).

[8] T. Havel, P. Cappellaro, C. Ramanathan, and D. G. Cory, in *Technical Proceedings of the 2005 NSTI Nanotechnology Conference and Trade Show* (NSTI, Danville, CA, 2005), Vol. 3, pp. 161–164.

[9] J. Kitching, S. Knappe, and E. Donley, IEEE Sens. J. **11**, 1749 (2011).

[10] F. Jelezko and J. Wrachtrup, Phys. Status Solidi A **203**, 3207 (2006).

[11] D. Le Sage, L. M. Pham, N. Bar-Gill, C. Belthangady, M. D. Lukin, A. Yacoby, and R. L. Walsworth, Phys. Rev. B **85**, 121202 (2012).
[12] J. M. Taylor, P. Cappellaro, L. Childress, L. Jiang, D. Budker, P. R. Hemmer, A. Yacoby, R. Walsworth, and M. D. Lukin, Nat. Phys. **4**, 810 (2008).
[13] L. Lust and D. Youngner, US Patent No. 7,359,059 (15 April 2008).
[14] T. G. Walker and W. Happer, Rev. Mod. Phys. **69**, 629 (1997).
[15] L. Robledo, H. Bernien, T. van der Sar, and R. Hanson, New J. Phys. **13**, 025013 (2011).
[16] G. Waldherr, J. Beck, M. Steiner, P. Neumann, A. Gali, T. Frauenheim, F. Jelezko, and J. Wrachtrup, Phys. Rev. Lett. **106**, 157601 (2011).
[17] G. Waldherr, J. Beck, P. Neumann, R. Said, M. Nitsche, M. Markham, D. J. Twitchen, J. Twamley, F. Jelezko, and J. Wrachtrup, Nat Nanotechnol. **7**, 105 (2012).
[18] G. D. Fuchs, G. Burkard, P. V. Klimov, and D. D. Awschalom, Nat. Phys. **7**, 789 (2011).
[19] V. Jacques, P. Neumann, J. Beck, M. Markham, D. Twitchen, J. Meijer, F. Kaiser, G. Balasubramanian, F. Jelezko, and J. Wrachtrup, Phys. Rev. Lett. **102**, 057403 (2009).
[20] B. Smeltzer, J. McIntyre, and L. Childress, Phys. Rev. A **80**, 050302 (2009).
[21] R. Fischer, A. Jarmola, P. Kehayias, and D. Budker, arXiv:1202.1072.
[22] S. R. Hartmann and E. L. Hahn, Phys. Rev. **128**, 2042 (1962).
[23] B. Luy and S. J. Glaser, Chem. Phys. Lett. **323**, 377 (2000).
[24] L. Childress and J. McIntyre, Phys. Rev. A **82**, 033839 (2010).
[25] J. H. Shirley, Phys. Rev. **138**, B979 (1965).
[26] G. D. Fuchs, V. V. Dobrovitski, D. M. Toyli, F. J. Heremans, and D. D. Awschalom, Science **326**, 1520 (2009).
[27] R. Hanson, V. V. Dobrovitski, A. E. Feiguin, O. Gywat, and D. D. Awschalom, Science **320**, 352 (2008).
[28] V. M. Acosta, E. Bauch, M. P. Ledbetter, C. Santori, K.-M. C. Fu, P. E. Barclay, R. G. Beausoleil, H. Linget, J. F. Roch, F. Treussart, S. Chemerisov, W. Gawlik, and D. Budker, Phys. Rev. B **80**, 115202 (2009).
[29] M. J. R. Hoch and E. C. Reynhardt, Phys. Rev. B **37**, 9222 (1988).
[30] A. Jarmola, V. M. Acosta, K. Jensen, S. Chemerisov, and D. Budker, Phys. Rev. Lett. **108**, 197601 (2011).
[31] L. Jiang, J. S. Hodges, J. R. Maze, P. Maurer, J. M. Taylor, D. G. Cory, P. R. Hemmer, R. L. Walsworth, A. Yacoby, A. S. Zibrov, and M. D. Lukin, Science **326**, 267 (2009).
[32] P. Neumann, J. Beck, M. Steiner, F. Rempp, H. Fedder, P. R. Hemmer, J. Wrachtrup, and F. Jelezko, Science **329**, 542 (2010).
[33] P. Cappellaro, Phys. Rev. A **85**, 030301(R) (2012).
[34] R. S. Said, D. W. Berry, and J. Twamley, Phys. Rev. B **83**, 125410 (2011).
[35] D. Budker and M. Romalis, Nat. Phys. **3**, 227 (2007).
[36] F. Dolde, H. Fedder, M. W. Doherty, T. Nobauer, F. Rempp, G. Balasubramanian, T. Wolf, F. Reinhard, L. C. L. Hollenberg, F. Jelezko, and J. Wrachtrup, Nat. Phys. **7**, 459 (2011).
[37] J. S. Hodges and D. Englund, arXiv:1109.3241.
[38] V. M. Acosta, E. Bauch, M. P. Ledbetter, A. Waxman, L.-S. Bouchard, and D. Budker, Phys. Rev. Lett. **104**, 070801 (2010).
[39] SAAB, 8088000-112 Fiber Optic Gyroscope (SAAB, Jönköping, Sweden, 2012), http://www.saabgroup.com/Global/Documents%20and%20Images/Land/Weapon%20Systems/FOG/FOG%20product%20sheet.pdf.
[40] Honeywell, GG1320AN Digital Ring Laser Gyro (Honeywell, Phoenix, 2012), http://www51.honeywell.com/aero/common/documents/myaerospacecatalog-documents/Missiles-Munitions/GG1320AN_Digital_Laser_Gyro.pdf.
[41] J. K. Stockton, K. Takase, and M. A. Kasevich, Phys. Rev. Lett. **107**, 133001 (2011).
[42] L. K. Lam, E. Phillips, E. Kanegsberg, and G. W. Kamin, Proc. SPIE **0412**, 272 (1983).
[43] B. J. Maertz, A. P. Wijnheijmer, G. D. Fuchs, M. E. Nowakowski, and D. D. Awschalom, Appl. Phys. Lett. **96**, 092504 (2010).
[44] S. Steinert, F. Dolde, P. Neumann, A. Aird, B. Naydenov, G. Balasubramanian, F. Jelezko, and J. Wrachtrup, Rev. Sci. Instrum. **81**, 043705 (2010).
[45] O. Auciello, S. Pacheco, A. Sumant, C. Gudeman, S. Sampath, A. Datta, R. Carpick, V. Adiga, P. Zurcher, Z. Ma, H.-C. Yuan, J. Carlisle, B. Kabius, J. Hiller, and S. Srinivasan, IEEE Microw. Mag. **8**, 61 (2007).
[46] S. Haykin, *Adaptive Filter Theory* (Prentice Hall, Englewood Cliffs, NJ, 2002).
[47] S. Pezzagna, B. Naydenov, F. Jelezko, J. Wrachtrup, and J. Meijer, New J. Phys. **12**, 065017 (2010).
[48] A. M. Edmonds, U. F. S. D'Haenens-Johansson, M. E. Newton, K.-M. C. Fu, C. Santori, R. G. Beausoleil, D. J. Twitchen, and M. L. Markham, Phys. Rev. B **86**, 035201 (2012).
[49] L. Robledo, L. Childress, H. Bernien, B. Hensen, P. F. A. Alkemade, and R. Hanson, Nature (London) **477**, 574 (2011).
[50] E. Togan, Y. Chu, A. Imamoglu, and M. D. Lukin, Nature (London) **478**, 497 (2011).
[51] A. M. Zagoskin, J. R. Johansson, S. Ashhab, and F. Nori, Phys. Rev. B **76**, 014122 (2007).
[52] J. R. Maze, P. L. Stanwix, J. S. Hodges, S. Hong, J. M. Taylor, P. Cappellaro, L. Jiang, A. Zibrov, A. Yacoby, R. Walsworth, and M. D. Lukin, Nature (London) **455**, 644 (2008).
[53] W. M. Witzel and S. Das Sarma, Phys. Rev. B **77**, 165319 (2008).
[54] N. Bar-Gill, L. Pham, C. Belthangady, D. Le Sage, P. Cappellaro, J. Maze, M. Lukin, A. Yacoby, and R. Walsworth, Nat. Commun. **3**, 858 (2012).
[55] W. M. Witzel, M. S. Carroll, L. Cywinski, and S. Das Sarma, Phys. Rev. B **86**, 035452 (2012).
[56] M. Ledbetter, K. Jensen, R. Fischer, A. Jarmola, and D. Budker, Phys. Rev. B **86**, 035201 (2012).
[57] D. Maclaurin, M. W. Doherty, L. C. L. Hollenberg, and A. M. Martin, Phys. Rev. Lett. **108**, 240403 (2012).